

The X-ray Emission of NGC 5005: An Unobscured Low-Luminosity AGN with a Weakly Accreting Broad-Line Region

ANNA TRINDADE FALCÃO,^{1,2} R. MIDDEI,^{2,3,4} G. FABBIANO,² M. ELVIS,² P. ZHU,² W. P. MAKSYM,⁵ D. Ł. KRÓL,² AND L. FEUILLET⁶

¹NASA-Goddard Space Flight Center, Code 662, Greenbelt, MD 20771, USA

²Harvard-Smithsonian Center for Astrophysics, 60 Garden St., Cambridge, MA 02138, USA

³INAF Osservatorio Astronomico di Roma, Via Frascati 33, 00078 Monte Porzio Catone, RM, Italy

⁴Space Science Data Center, Agenzia Spaziale Italiana, Via del Politecnico snc, 00133 Roma, Italy

⁵NASA Marshall Space Flight Center, Huntsville, AL 35812, USA

⁶Institute for Astrophysics and Computational Sciences

and Department of Physics, The Catholic University of America,
Washington, DC 20064, USA

ABSTRACT

We present deep *Chandra* X-ray observations of NGC 5005, a LINER-dominated galaxy previously reported to host a broad H α emission line. The diffuse soft X-ray emission (<3 keV) extends out to \sim 800 pc, while harder emission (>3 keV) is confined to the central \sim 400 pc. Spatially resolved spectroscopy of the nuclear ($r < 150$ pc) and extended ($150 < r < 500$ pc) regions reveals that these are best described by models including both photoionized and thermal plasma components, **consistent with excitation by a low-luminosity AGN and shock-heated gas**. Narrow-band imaging and excitation maps from the *Hubble Space Telescope* (*HST*) support this interpretation, closely matching the X-ray morphology and ionization structure. The detection of a faint hard X-ray nuclear source with *Chandra*, combined with stringent upper limits from *NuSTAR* and *Swift*, and consistency with the X-ray luminosity predicted from the *HST* [O III] λ 5007 emission, indicates that NGC 5005 hosts an intrinsically low-luminosity ($L_{\text{bol}} \sim 10^{41}$ erg s⁻¹), unobscured AGN. Despite the extremely low Eddington ratio inferred from our measurements ($\lambda_{\text{Edd}} \sim 5 \times 10^{-6}$), the presence of a broad H α line in the optical spectrum suggests the persistence of a thin accretion disk, challenging standard paradigms of accretion flow configurations at such low accretion rates.

Keywords: LINER galaxies, NGC 5005

1. INTRODUCTION

This paper is the second in our series on the LINER active galactic nucleus (AGN) galaxy NGC 5005, and the first to present results based on deep *Chandra* observations of its nuclear region. NGC 5005 is a weakly barred spiral galaxy [SAB(r)] with a dust-enshrouded nucleus (Pogge et al. 2000), located at a distance of $D \sim 17$ Mpc (NED; $z=0.003156$, scale = 100 pc arcsec⁻¹).

Early optical observations revealed strong nuclear emission lines, including [O II], [O III], H α , and [S II] (Shuder & Osterbrock 1981), but did not establish a definitive AGN classification. While initially considered unlikely to be a Seyfert 2, subsequent studies have variously classified NGC 5005 as a low-ionization nuclear emission-line region (LINER; Huchra

& Burg 1992; Ho et al. 1997; Véron-Cetty & Véron 2006), a Seyfert 2 galaxy (Audibert et al. 2017), or a hybrid of both types (Spinelli et al. 2006; Malkan et al. 2017).

Spectroscopy from the Palomar survey identified a broad H α component blended with narrow H α and [N II] lines, suggesting the presence of an unobscured AGN (Rush et al. 1996; Ho et al. 1997). However, follow-up *Hubble Space Telescope* (*HST*) spectroscopy using the [O I] line for deblending did not confirm the broad component. This led Balmaverde & Capetti (2014) to propose either a misidentification or a possible changing-look AGN. In contrast, Constantin et al. (2015) detected a broad H α component (FWHM = 2,610 km s⁻¹) using [S II] as the deblending template. Cazzoli et al. (2018) later confirmed the presence of a weak broad H α line (FWHM = 2,152 km s⁻¹) in the *HST* data, although it remained undetected in ground-based spectra.

The presence of a Compton-thick (CT) AGN was initially proposed by Risaliti et al. (1999) based on a low 2–10 keV

to [O III] luminosity ratio. However, their *ASCA* spectrum lacked a strong 6.4 keV Fe K α line, placing an upper limit of 900 eV on its equivalent width (EW). This led to the interpretation that soft X-rays were fully obscured and the observed spectrum was dominated by star-formation-related emission.

Subsequent observations with *Chandra* and *XMM-Newton* detected extended soft X-ray emission aligned with the galaxy disk (Guainazzi et al. 2005), likely contributing to the excess emission observed around 0.6–1 keV (Gallo et al. 2006). Guainazzi et al. (2005) ruled out an inverse Compton origin for the soft component, placing a tighter upper limit of 240 eV on the Fe K α EW, and favored a significantly lower absorbing column ($N_{\text{H}} \sim 1.5 \times 10^{20} \text{ cm}^{-2}$), revising the CT interpretation. Later studies reported N_{H} values in the range of 10^{20} – 10^{21} cm^{-2} (Brightman & Nandra 2011; Younes et al. 2011).

In Trindade Falcão et al. (2025), we analyzed continuum-subtracted *HST* narrow-line images to explore the spatially resolved excitation structure in the narrow-line region (NLR) of NGC 5005. We identified a compact (~ 100 pc) nuclear Seyfert-like zone, likely photoionized by the AGN, surrounded by a higher ionization LINER-like cocoon indicative of shock excitation in the interstellar medium (ISM). Additional LINER-like emission extends across the central kiloparsec, consistent with ionization from a low-luminosity AGN. We also detected H II (star-forming)-like regions within the inner 500 pc, possibly arising from jet–ISM interactions, and in a star-forming ring at $r \sim 4$ kpc.

In this paper, we examine the nuclear and extended X-ray emission of NGC 5005 using the full 255 ks of archival *Chandra* ACIS-S observations, in combination with archival *NuSTAR* and *Swift* data. We focus on the spatial and spectral properties of the X-ray emission to assess the AGN’s luminosity, absorption properties, and its role in exciting the surrounding ISM. Section 2 describes the observations, data reduction, and analysis procedures. In Sections 3 and 4, we present results from imaging and spectral analysis, respectively. Section 5 discusses the implications of our findings, and Section 6 summarizes our conclusions.

NGC 5005 thus offers a uniquely valuable case for probing the duty cycle and feedback signatures of LINER-type AGNs. Its comparatively faint X-ray nucleus ($L_{\text{X}} \sim 10^{40} \text{ erg s}^{-1}$; González-Martín et al. 2009) contrasts with its luminous [O III] emission (Trindade Falcão et al. 2025), raising long-standing questions about the true nature of the central source. This ambiguity, combined with its proximity ($D \sim 17$ Mpc), allows *Chandra* to resolve ~ 30 pc scales and directly connect nuclear activity to circumnuclear excitation. Equally important, NGC 5005 is exceptionally well studied across the spectrum, with available *HST* narrow-band imaging, radio jet detections (Baldi et al. 2018), circumnuclear CO structures (Sakamoto et al. 2000), and rich optical/IR data on

dust, gas, and star formation (e.g., Pogge et al. 2000; Asmus et al. 2014). These factors make it a natural choice for a detailed case study, providing both technical advantages and a pioneering framework for broader population studies of LINER-dominated systems.

2. OBSERVATIONS, DATA REDUCTION, AND ANALYSIS

2.1. *Chandra* Observations

Table 1 summarizes the X-ray observations analyzed in this study. NGC 5005 was observed a total of sixteen times with *Chandra*, primarily during the 2022–2023 observing campaign, resulting in a cumulative exposure of ~ 255 ks. All *Chandra* datasets used in this work are publicly available through the *Chandra* Data Collection (CDC) 358 doi:10.25574/cdc.358.

Data reduction was carried using CIAO 4.17¹ (Fruscione et al. 2006), following standard procedures. Each observation was reprocessed with the `chandra_repro`² script, which applies the latest calibrations and enables sub-pixel resolution capabilities specific to ACIS-S.

For imaging analysis, individual datasets were aligned and merged using ObsID 25698, the longest single exposure, as the astrometric reference. Full-band (0.3–7 keV) images from each observation were visually inspected to check alignment quality. Centroid shifts between datasets were measured using the CIAO tool `dmstat`³, applied to 0.3–7 keV images binned at 1/8 the native pixel size. Centroids were calculated within a $r = 0.2''$ circular region centered on the brightest pixel. All observed centroid shifts were smaller than the native ACIS-S pixel scale of $0.492''$.

To ensure astrometric consistency across exposures, we cross-matched additional point sources and corrected any residual offsets using `wcs_update`⁴. Updated aspect solutions were incorporated using `reproject_obs`⁵, and final merged datasets were generated with `merge_obs`⁶. Merged images in the full (0.3–7 keV), soft (0.3–3 keV), and hard (3–7 keV) energy bands are shown in Figure 1. These images were binned at 1/8 of the native pixel scale and smoothed with a 3-pixel Gaussian kernel to take advantage of sub-pixel event repositioning, enhancing spatial detail for high-resolution morphological analysis while suppressing pixel-scale noise fluctuations.

2.2. Archival *Swift* and *NuSTAR* Observations

¹ <https://cxc.cfa.harvard.edu/ciao/>

² https://cxc.cfa.harvard.edu/ciao/ahelp/chandra_repro.html

³ <https://cxc.cfa.harvard.edu/ciao/ahelp/dmstat.html>

⁴ https://cxc.cfa.harvard.edu/ciao/ahelp/wcs_update.html

⁵ https://cxc.cfa.harvard.edu/ciao/ahelp/reproject_obs.html

⁶ https://cxc.cfa.harvard.edu/ciao/ahelp/merge_obs.html

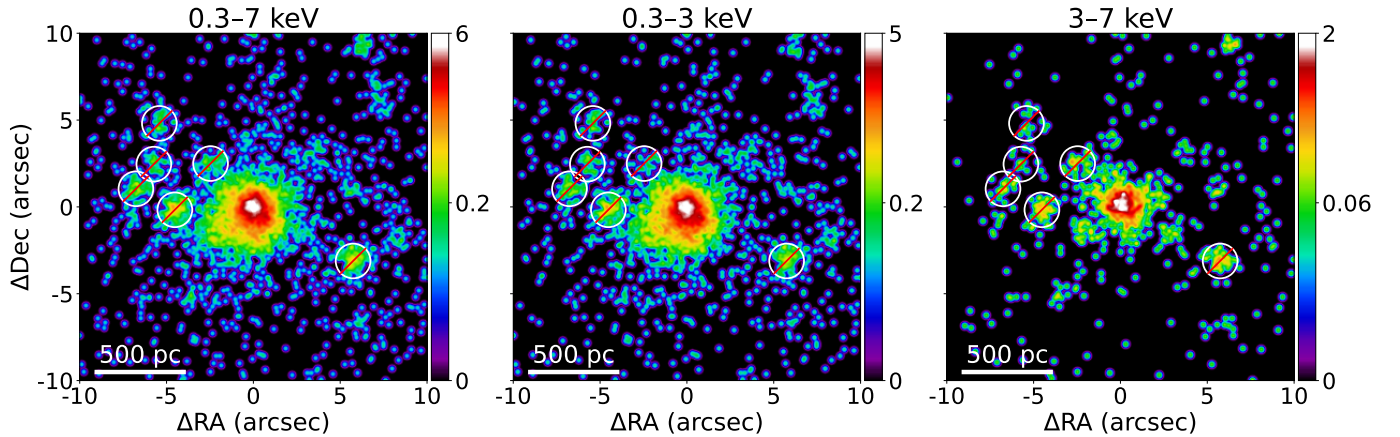


Figure 1. Merged 1/8 subpixel *Chandra*/ACIS-S images of NGC 5005, smoothed with a 3-pixel Gaussian kernel and shown in the indicated energy bands. Non-nuclear point sources, which were excluded from the spatial and spectral analysis, are marked. In this and all other images displayed in this paper, north is up and east is to the left, with color bars shown in units of counts.

NGC 5005 was observed with *NuSTAR* (Harrison et al. 2013) on December 16, 2014 (ObsID: 60001162002), with a total exposure time of approximately 50 ks. A short follow-up snapshot was obtained by *Swift* (Gehrels et al. 2004) on December 19, 2014, with a total exposure of ~ 2 ks. The *NuSTAR* FPMA and FPMB data were analyzed in the 3–30 keV band, while the *Swift*-XRT data were examined over the 0.5–4 keV range. Details of both observations are listed in Table 1.

NuSTAR data reduction was performed using the NUSTARDAS⁷ software package with the latest calibration files available as of April 15, 2025. Science products were generated with the `nuproducts` task for both focal plane modules (FPMA and FPMB). The source spectrum was extracted from a circular region of radius $30''$ centered on the nucleus of NGC 5005. A background spectrum was extracted from a nearby source-free region of equal size. Spectra were grouped to ensure a minimum of five counts per bin.

The *Swift*-XRT exposure was processed using the automated pipeline provided by the Space Science Data Center (SSDC) of the Italian Space Agency. We used their interactive interface to reduce, calibrate, and clean the dataset, and to extract both source and background spectra. The source region was defined as a circle with radius $20''$ centered on the AGN, while the background was extracted from an adjacent annulus with a width of $10''$, positioned to sample a blank region. The resulting spectrum was grouped to contain at least three counts per bin.

3. IMAGING ANALYSIS AND RESULTS

3.1. Modeling the *Chandra* PSF

To accurately model the *Chandra* point spread function (PSF), we simulated individual PSFs for each of the *Chandra* exposures listed in Table 1. These simulations were carried

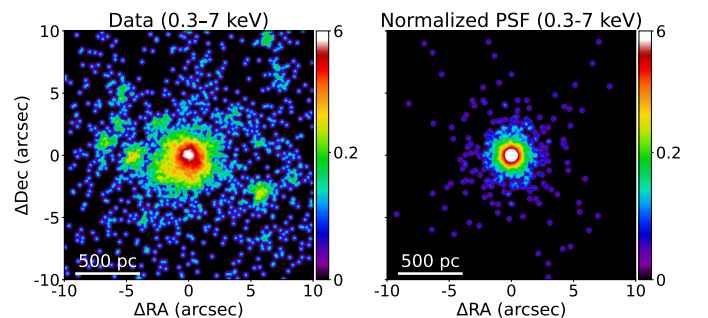


Figure 2. *Left:* Merged *Chandra* 0.3–7 keV image of NGC 5005, as shown in Figure 1. *Right:* Simulated PSF generated with MARX, scaled to match the total number of counts within the central $1.5''$ radius. Both panels are displayed with the same color scale, binning (1/8 pixel), and Gaussian smoothing to enable direct comparison.

out using CHART⁸, which accounts for the input source spectrum, off-axis angle, and aspect solution of each observation. The simulated ray traces were then projected onto the ACIS-S detector using MARX⁹, which incorporates parameters such as observation date, detector position, and exposure time.

To minimize pixelation effects in the final PSF model, we set the ASPECTBLUR parameter to 0.19, as recommended for ACIS-S data¹⁰. Each individual CHART simulation was converted into an event file after projection. These simulated PSF event files were then combined using `dmmerge`¹¹ to create a single, composite PSF suitable for use in our imaging analysis.

All simulations were registered to a common astrometric frame using ObsID 25698 as the reference. Finally, the composite PSF was normalized to match the total source counts

⁸ <https://cxc.cfa.harvard.edu/ciao/PSFs/chart2/index.html>

⁹ <https://space.mit.edu/cxc/marx/>

¹⁰ <https://cxc.cfa.harvard.edu/ciao/why/aspectblur.html>

¹¹ <https://cxc.cfa.harvard.edu/ciao/ahelp/dmmerge.html>

⁷ https://heasarc.gsfc.nasa.gov/docs/nustar/analysis/nustar_swguide.pdf

Table 1. X-ray Observations of NGC 5005 used in this work.

Obs ID	Date	Exposure (ks)	PI
<i>Chandra ACIS-S</i>			
4021	2003-08-19	5.0	Satyapal
25255	2023-07-19	15.0	Fabbiano
25694	2023-08-06	14.0	Fabbiano
25695	2022-08-09	14.0	Fabbiano
25696	2023-03-04	12.0	Fabbiano
25697	2023-08-06	10.0	Fabbiano
25698	2023-06-16	44.0	Fabbiano
25699	2023-06-18	16.0	Fabbiano
25700	2023-05-12	30.0	Fabbiano
27251	2022-08-11	14.0	Fabbiano
27252	2023-08-12	10.5	Fabbiano
27958	2023-07-19	14.0	Fabbiano
27976	2023-08-22	16.0	Fabbiano
28372	2023-08-12	12.0	Fabbiano
28493	2023-08-22	18.5	Fabbiano
28494	2023-08-23	10.0	Fabbiano
<i>NuSTAR FPMA/FPMB</i>			
6000116200	2014-12-16	50.0	Harrison
<i>Swift XRT</i>			
00080825002	2014-12-19	2.0	Swift

within a circular region of radius $r = 1.5''$ centered on the nucleus of NGC 5005.

Figure 2 displays a side-by-side comparison of the observed *Chandra* image and the simulated, normalized PSF model in the 0.3–7 keV band. Both images use identical binning, smoothing, and color scales for direct visual comparison.

3.2. Azimuthal and Radial Dependence of the Extended X-ray Emission

The merged *Chandra* images presented in Figure 1 reveal a bright nuclear point source surrounded by diffuse circumnu-

clear X-ray emission extending out to $r \sim 5''$ (500 pc), with a roughly circular morphology. To isolate and characterize the extended component, we first identified point sources in the field using the `wavdetect`¹² algorithm with scale parameters of 1, 2, 4, 8, and 16 pixels.

Several point sources were detected across the field of view. These sources were excluded from both the spatial and spectral analysis. Their corresponding pixels were replaced using the `dmfilth`¹³ tool, which interpolates pixel values from surrounding regions at comparable radial distances from the nucleus. The regions affected by the point sources were also masked from subsequent measurements.

After excluding the point sources, we detect 4752 ± 69 net counts above the background within a $5''$ radius from the centroid of the 0.3–7 keV emission (see Table 2). The X-ray emission in this region is dominated by soft photons, with only 943 ± 31 net counts detected at energies above 3 keV, indicating that the diffuse emission is primarily soft in nature.

To investigate potential directional asymmetries in the extended emission and assess their dependence on photon energy, we constructed azimuthal surface brightness profiles in several narrow X-ray energy bands. These profiles were extracted from both the observed data and energy-matched PSF simulations. The extraction regions consisted of pie-shaped sectors extending from $r = 1.5''$ to $r = 8''$, centered on the centroid of the 0.3–7 keV image, and divided into 10° angular bins (see Figure 3, left). Point sources were excluded in all cases. The simulated PSF profiles were normalized to match the source counts within the innermost ($r < 1.5''$) region. The middle panels of Figure 4 show a direct comparison between the observed data (shown in red) and PSF (in black) azimuthal profiles.

To further quantify the extent of the diffuse emission, we constructed radial surface brightness profiles in each energy band and compared them with the corresponding PSF models. The right-hand panels of Figure 4 present the background-subtracted radial profiles from the merged dataset (shown in red), overlaid with the simulated PSF profiles (in black). All profiles were extracted from a circular region of radius $r = 8''$, centered on the centroid of the full-band image, and divided into 20 concentric annuli (see Figure 3, right). The PSF simulations incorporate the exposure times of the individual observations (Table 1), so the model profiles include the expected level of statistical uncertainty.

3.3. Spatial Properties of the Extended X-ray Emission

As illustrated in Figure 4, the soft X-ray emission (energies < 3 keV) is the most spatially extended component. Radial surface brightness profiles in the 0.3–1.5 keV and 1.5–3 keV

¹² <https://cxc.cfa.harvard.edu/ciao/ahelp/wavdetect.html>

¹³ <https://cxc.cfa.harvard.edu/ciao/ahelp/dmfilth.html>

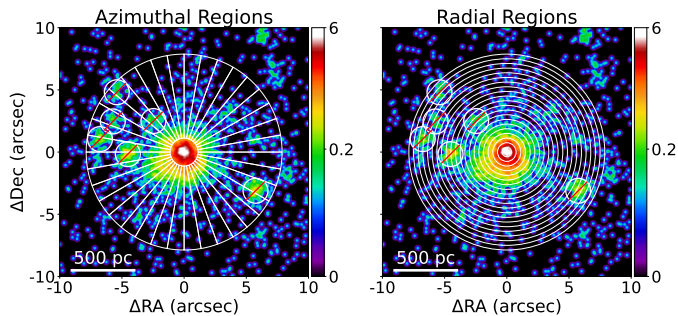


Figure 3. *Left panel:* *Chandra* full-band image with overlaid pie-shaped extraction regions spanning radii of $1.5''$ – $8''$ and divided into 36 angular bins (10° each), used to extract azimuthal surface brightness profiles from the merged data and simulated PSF model. *Right panel:* Same image with 20 overlaid concentric annuli used to extract radial surface brightness profiles from a $r = 8''$ region.

bands show emission reaching out to $r \sim 8''$ (800 pc) from the nuclear centroid. These profiles clearly exceed that of the simulated PSF, indicating the presence of diffuse, extended emission in these bands. The corresponding azimuthal profiles (middle column of Figure 4) show that the soft X-ray emission is preferentially enhanced in the 180° – 360° range relative to the PSF, with excess emission extending toward the southeast (SE), south (S), and southwest (SW) directions.

We also analyzed the spatial properties of the emission in the 3–4 keV and 4–5 keV bands, which yield 2748 ± 52 and 1562 ± 40 net counts, respectively, within a circular region of radius $r = 8''$. After subtracting the PSF contribution, the residual extended emission in these bands corresponds to 671 ± 26 and 436 ± 21 counts, respectively (see Table 2). The radial profiles in both bands show significant emission extending out to $r \sim 6''$ – $7''$ (600–700 pc). However, unlike the soft bands, the azimuthal profiles in these higher energy ranges do not show strong directional asymmetries.

As the photon energy increases, the spatial extent of the X-ray emission decreases, while the azimuthal profiles remain relatively flat. The emission in the 5–6 keV band extends to $r \sim 7''$ (700 pc), whereas the 6–7 keV emission is confined to within $r \sim 4''$ (400 pc) of the nuclear centroid.

Notably, the radial profiles at all energies (Figure 4, right) do not decline to zero at large radii, even in the highest energy bands. This suggests the presence of a pervasive diffuse X-ray component throughout the galaxy. Supporting this interpretation, Figure 5 compares the full-band *Chandra* image with contours from the *HST* F814W wide-band continuum filter, revealing that the *Chandra* field of view is largely filled by the host galaxy. The integrated X-ray emission from unresolved sources, such as X-ray binaries, supernova remnants, stellar populations, and hot ISM, likely contributes to the observed diffuse excess. A detailed analysis of this galaxy-wide emission component is beyond the scope of this work.

Table 2. Excess Net Counts Above Model PSF

Band (keV)	$r < 8''$	$1.5'' < r < 8''$
0.3–1.5	4537 ± 67	375 ± 19
1.5–3.0	3639 ± 60	159 ± 13
3.0–4.0	671 ± 26	75 ± 9
4.0–5.0	436 ± 21	60 ± 8
5.0–6.0	293 ± 17	26 ± 5
6.0–7.0	172 ± 13	15 ± 4

In summary, the radial surface brightness analysis indicates that the extended emission reaches out to ~ 800 pc at energies below 3 keV, declines to ~ 600 – 700 pc in the 3–6 keV range, and is restricted to ~ 400 pc at 6–7 keV. While the soft-band emission shows directional enhancements toward the SE, S, and SW, the higher-energy emission appears more isotropic.

4. SPECTRAL ANALYSIS AND RESULTS

Guided by the azimuthal and radial surface brightness profiles presented in Figure 4, we extracted spectra from two distinct regions: (1) a circular region with radius $r = 1.5''$ (150 pc), centered on the centroid of the 0.3–7 keV emission, to isolate the nuclear and immediate circumnuclear emission (hereafter referred to as the *core* spectrum); and (2) an annular region spanning $r = 1.5''$ – $5''$ (150–500 pc), to isolate the extended circumnuclear emission (hereafter the *extended* spectrum). These extraction regions are shown in the left panel of Figure 6.

Spectra for each of the sixteen individual *Chandra* exposures (see Table 1) were extracted using the CIAO tool `specextract`¹⁴. A circular background region of radius $r = 10''$, free of point sources and located on the same CCD chip, was used for background subtraction. The resulting source and background spectra, as well as the corresponding response files, were combined across all observations using the `combine_spectra`¹⁵ tool. The final spectra were grouped to contain a minimum of 10 counts per bin to ensure robust spectral fitting.

Spectral modeling was carried out using `XSPEC`¹⁶, adopting physically motivated models appropriate for AGN and circumnuclear emission components, as detailed in the subsections below.

¹⁴ <https://cxc.cfa.harvard.edu/ciao/ahelp/specextract.html>

¹⁵ https://cxc.cfa.harvard.edu/ciao/ahelp/combine_spectra.html

¹⁶ <https://heasarc.gsfc.nasa.gov/xanadu/xspec/>

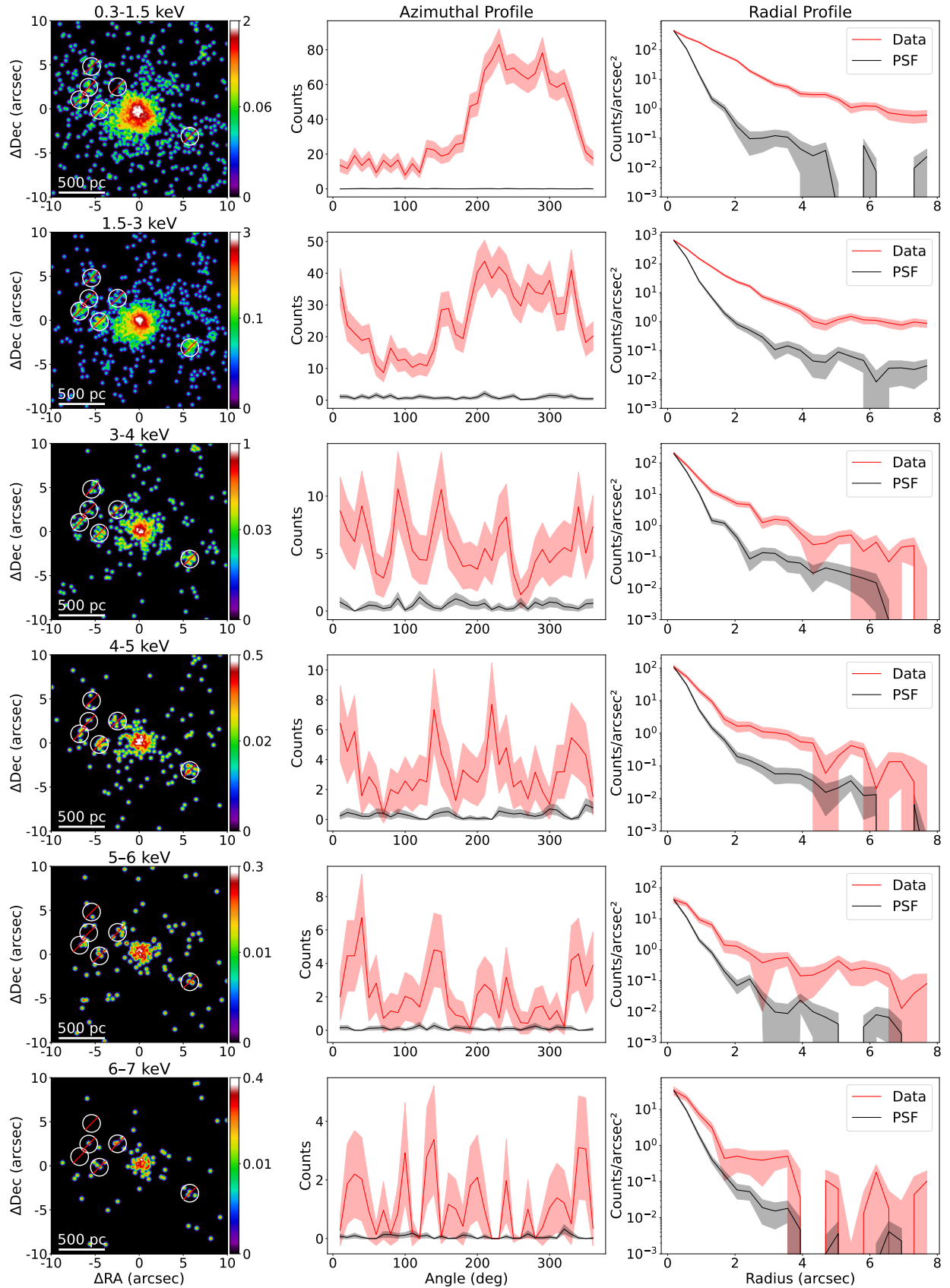


Figure 4. Images (left column), azimuthal surface brightness profiles (middle column, 0° corresponds to West), and radial surface brightness profiles (right column) of NGC 5005 in different energy bands. The images were rebinned to $1/8$ of the native ACIS pixel scale and smoothed with a 3-pixel Gaussian. The PSF in each band was normalized to match the source counts in the innermost region.

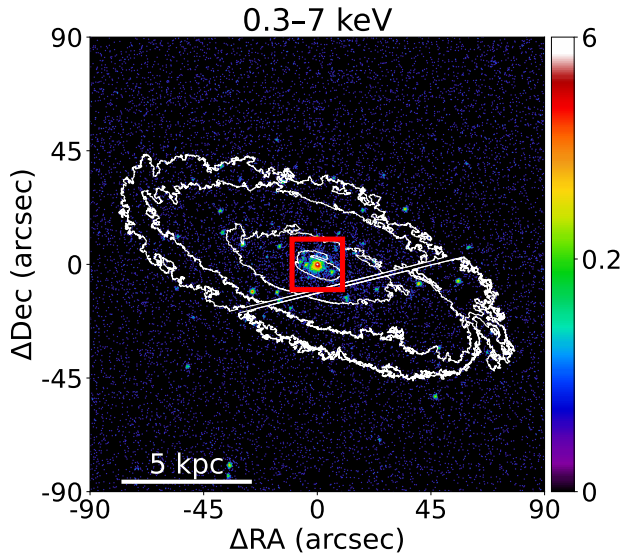


Figure 5. Full-band *Chandra* image of NGC 5005, rebinned to 1/8 of the native ACIS pixel scale. White contours show the *HST* F814W wide-band image. The diffuse X-ray excess detected in the data (see radial profiles in Figure 4) likely includes contributions from unresolved sources in the galaxy, such as X-ray binaries, supernova remnants, stellar sources, and hot interstellar medium. The red square has dimensions of $5'' \times 5''$, as in Figure 4, for comparison.

4.1. Spectral Modeling

To investigate the dominant emission mechanisms in each spatial region, we employed a physically motivated modeling approach incorporating both photoionized and collisionally ionized plasma components. Photoionized emission was modeled using precomputed grids generated with *Cloudy*¹⁷ (Ferland et al. 2017), while thermal emission was modeled using the *APEC*¹⁸ plasma code (Foster et al. 2012).

Each extracted spectrum was initially fit with a single emission component. Additional components were introduced only when justified by statistically significant residuals and improvements in the fit statistic. Model adequacy was evaluated using both the C-statistic per degree of freedom (Cstat/d.o.f.) and visual inspection of residuals. In cases where Cstat/d.o.f. ~ 1 but structured residuals remained, additional physically motivated components were incorporated.

4.1.1. Photoionized and Thermal Emission Components

The photoionized gas was modeled using additive emission components derived from *Cloudy* c13.01 grids. These models assume an input spectral energy distribution (SED) of the form $L_\nu \propto \nu^{-\alpha}$, with $\alpha = 0.5$ for $1 \times 10^{-4} \text{ eV} < h\nu < 13.6 \text{ eV}$ and $\alpha = 1.0$ for $13.6 \text{ eV} < h\nu < 30 \text{ keV}$. Solar elemental abundances were adopted throughout. The model grid spans

ionization parameters in the range $\log U = -2$ to 4 (in steps of 0.25 dex) and hydrogen column densities from $\log N_{\text{H}} = 19$ to 23.5 (in steps of 0.1 dex). These grids were converted into XSPEC-compatible additive tables following the procedure described in Porter et al. (2006).

Collisionally ionized thermal emission was modeled using *APEC*, assuming solar abundances. This component accounts for hot, diffuse gas possibly heated by AGN-driven winds or radio jets, or by stellar processes such as supernovae and star formation (e.g., Fabbiano et al. 2018; Travescio et al. 2021; Trindade Falcão et al. 2023).

4.2. Spectral Properties of the X-ray Emission

The results of the spectral modeling for each *Chandra* spectra are summarized in Table 3, with the extraction regions shown in the left panel of Figure 6. All fits include foreground Galactic absorption fixed at $N_{\text{H}} = 1.18 \times 10^{20} \text{ cm}^{-2}$, as determined using the NASA HEASARC tool¹⁹.

4.2.1. The Core Spectrum

The core spectrum (Figure 7, left) is dominated by soft X-ray emission below 3 keV, but also shows evidence of hard X-ray features, including a possible neutral Fe $K\alpha$ line at $E_{\text{rest}} = 6.4 \text{ keV}$. To model this high-energy component, we adopted the physically motivated torus model *MYTorus*²⁰ (Murphy & Yaqoob 2009), which simulates X-ray reprocessing in a toroidal distribution of neutral material. Specifically, we included the scattered continuum (*mytS*, shown in cyan) and fluorescent line (*mytL*, shown in pink) components, to account for reprocessed hard X-ray emission and iron line fluorescence.

To identify regions dominated by line emission, we first performed a phenomenological fit to the soft X-ray band using several redshifted Gaussian components with fixed width $\sigma = 0.1 \text{ keV}$, matching the spectral resolution of the ACIS-S detector. Line centroids and normalizations were allowed to vary freely. This model also included foreground absorption via *tbabs*. The results of this fit are shown in the top-left panel of Figure 7. We emphasize that this approach is not intended for deriving physical quantities of the gas, especially below 1.5 keV where spectral blending is significant at the resolution of ACIS.

This analysis reveals four prominent emission features in the core spectrum, with fitted centroid energies of $E_{\text{rest}} = 0.94 \pm 0.01 \text{ keV}$, $1.35 \pm 0.02 \text{ keV}$, $1.84 \pm 0.02 \text{ keV}$, and $2.40 \pm 0.03 \text{ keV}$. These likely correspond to blended line complexes of Ne IX+Ne X, Mg XI+Mg XII, Si XIII+Si XIV, and S XV, respectively (e.g., Trindade Falcão et al. 2023).

¹⁷ <http://www.nublado.org/>

¹⁸ <http://www.atomdb.org/>

¹⁹ <https://heasarc.gsfc.nasa.gov/>

²⁰ <https://www.mytorus.com/>

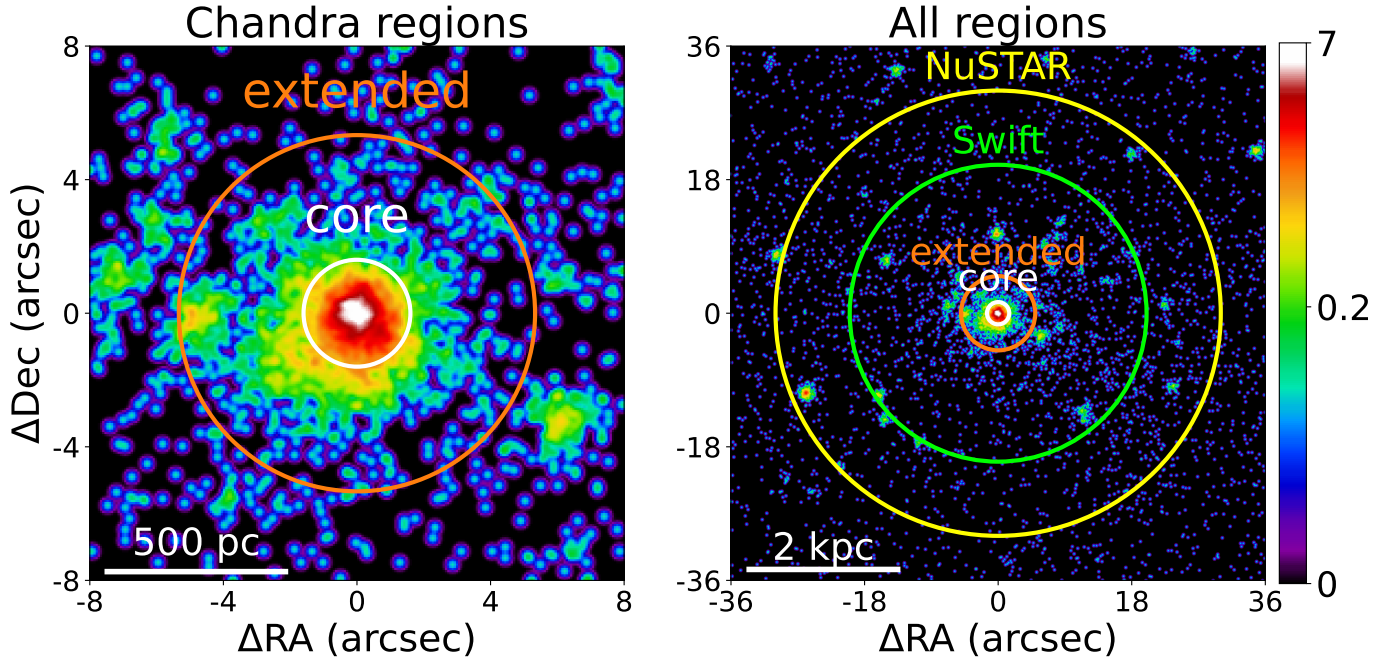


Figure 6. *Left:* *Chandra* ACIS-S image of the 0.3–7 keV emission, rebinned to 1/8 of the native pixel scale and smoothed with a Gaussian kernel ($\sigma = 1.5$ pixels). The inner white circle ($r = 1.5''$) marks the *Chandra* core extraction region, while the surrounding orange annulus ($1.5'' < r < 5''$) corresponds to the extended emission region analyzed in Section 4. *Right:* Same as in the left panel, but with the outer green annulus indicating the *Swift* extraction region ($r = 20''$), while the outermost yellow annulus corresponds to the *NuSTAR* extraction region ($r = 30''$).

We then proceed to fit the full core spectrum using a physically motivated model that combines photoionized gas (modeled with *CLOUDY*) and collisionally ionized plasma (modeled with *APEC*). The photon index for both *mytS* and *mytL* components was fixed at $\Gamma = 1.8$, and their column densities were linked but allowed to vary. The inclination angle was fixed at 0° . The best-fit model (Cstat/d.o.f. = 1.04; shown in lime green in Figure 7) yields a line-of-sight column density of $N_{\text{H}} = (3.7 \pm 0.3) \times 10^{21} \text{ cm}^{-2}$, consistent with previous studies (González-Martín et al. 2009; Younes et al. 2012).

The best-fit model (Figure 7, bottom-left panel) indicates that the soft X-ray emission in the core is best described by a combination of a low-ionization photoionized component ($\log U = -0.11 \pm 0.11$, $\log N_{\text{H}} = 21.00 \pm 0.22 \text{ cm}^{-2}$; shown in blue) and a thermal plasma with $kT = 0.90 \pm 0.05 \text{ keV}$ (shown in red). Table 3 reports the corresponding model luminosities for each component in the 0.3–7 keV band. The observed and intrinsic 2–10 keV X-ray luminosities derived from the model are $L_{\text{obs}} = (2.67 \pm 0.46) \times 10^{39} \text{ erg s}^{-1}$ and $L_{\text{int}} = (2.77 \pm 0.46) \times 10^{39} \text{ erg s}^{-1}$, respectively.

4.2.2. The Extended Spectrum

As shown in Figure 4, extended X-ray emission is detected out to $r \sim 800 \text{ pc}$, particularly at energies below 3 keV. In obscured AGNs, such soft X-ray emission is commonly associated with [O III] $\lambda 5007$ and is typically attributed to AGN photoionization, though contributions from collision-

ally ionized plasma may also be present (e.g., Fabbiano & Elvis 2024).

The spectrum extracted from the extended region of NGC 5005 is shown in the right panels of Figure 7. To model the hard continuum, we included a reflection component using *peXrav* (shown in purple), assuming a power-law slope of $\Gamma = 1.8$, an exponential cutoff energy of $E_{\text{fold}} = 1,000 \text{ keV}$, and an inclination cosine of $\cos(i) = 0.5$.

As with the core spectrum, we first applied a phenomenological model to identify dominant emission lines in the soft band. This model included several redshifted Gaussian components (in orange) with fixed widths of $\sigma = 0.1 \text{ keV}$ and variable centroid energies and normalizations. The result of this fit is shown in the top-right panel of Figure 7. The extended spectrum exhibits strong emission features at $E_{\text{rest}} = 0.77 \pm 0.03 \text{ keV}$, $1.03 \pm 0.03 \text{ keV}$, $1.39 \pm 0.03 \text{ keV}$, and $1.83 \pm 0.03 \text{ keV}$. These features likely correspond to blended emission from O VIII+Fe XVII, Ne IX+Ne X, Mg XI+Mg XII, and Si XIII+Si XIV, respectively.

We then fit the full extended spectrum using a combination of photoionized and thermal plasma components, as described in Section 4.1.1. The best-fit model (Cstat/d.o.f. = 1.13; shown in lime green in Figure 7) includes a low-ionization photoionized component with $\log U = -0.76 \pm 0.35$ and $\log N_{\text{H}} = 19.37 \pm 0.24 \text{ cm}^{-2}$ (shown in blue), along with a collisionally ionized thermal component with $kT = 0.89 \pm 0.05 \text{ keV}$ (shown in red).

Table 3. Best-fit Spectral Components and Parameters for NGC 5005

Component	Physical Component	Parameter	Value	$L_{0.3-7 \text{ keV}}$
Core Region (Cstat/d.o.f. = 1.04)				
TBabs	Foreground absorption	N_{H}	0.37 ± 0.03	–
apec	Collisionally-ionized gas	kT	0.90 ± 0.05	–
apec	Collisionally-ionized gas	norm	$(7.37 \pm 1.02) \times 10^{-5}$	39.68 ± 0.03
CLOUDY	Photoionized gas	$\log U$	-0.11 ± 0.11	–
CLOUDY	Photoionized gas	$\log N_{\text{H}}$	21.00 ± 0.22	–
CLOUDY	Photoionized gas	norm	$(1.10 \pm 1.25) \times 10^{-14}$	39.84 ± 0.10
mytL	Fluorescent lines (torus)	N_{H}	<2.00	–
mytL	Fluorescent lines (torus)	norm	$(2.58 \pm 1.15) \times 10^{-3}$	37.81 ± 0.20
mytS	Scattered AGN continuum (torus)	norm	$(8.37 \pm 1.02) \times 10^{-3}$	39.14 ± 0.06
Extended Region (Cstat/d.o.f. = 1.13)				
apec	Collisionally-ionized plasma	kT	0.89 ± 0.05	–
apec	Collisionally-ionized plasma	norm	$(1.89 \pm 0.56) \times 10^{-5}$	39.09 ± 0.03
CLOUDY	Photoionized gas	$\log U$	-0.76 ± 0.35	–
CLOUDY	Photoionized gas	$\log N_{\text{H}}$	19.37 ± 0.24	–
CLOUDY	Photoionized gas	norm	$(4.20 \pm 2.00) \times 10^{-13}$	38.92 ± 0.13
pexrav	Reflected AGN continuum (disk/slab)	norm	$(6.11 \pm 1.32) \times 10^{-6}$	38.84 ± 0.07
NuSTAR–Swift (Cstat/d.o.f. = 0.88)				
TBabs	Foreground absorption	N_{H}	0.37^{\dagger}	–
apec	Collisionally-ionized plasma	kT	0.90^{\dagger}	–
apec	Collisionally-ionized plasma	norm	$< 1.2 \times 10^{-4}$	39.83 ± 0.14
CLOUDY	Photoionized gas	$\log U$	-0.11^{\dagger}	–
CLOUDY	Photoionized gas	$\log N_{\text{H}}$	21.00^{\dagger}	–
CLOUDY	Photoionized gas	norm	$(5.6 \pm 2.6) \times 10^{-14}$	< 39.78
mytL	Fluorescent lines (torus)	N_{H}	$<2.00^{\dagger}$	–
mytL	Fluorescent lines (torus)	norm	$(1.17 \pm 0.07) \times 10^{-2}$	38.64 ± 0.20
mytS	Scattered AGN continuum (torus)	norm	$< 4.1 \times 10^{-2}$	39.65 ± 0.25

Note: N_{H} is in units of 10^{22} cm^{-2} , kT in keV, and luminosities are in $\log \text{ erg s}^{-1}$. "norm" refers to the XSPEC normalization of each component. CLOUDY and apec represent photoionized and thermal gas, respectively. mytS and mytL are reprocessed continuum and line emission from a toroidal AGN structure. The \dagger symbols identify the parameters that were frozen during the fitting process, see Section 4.3 for details.

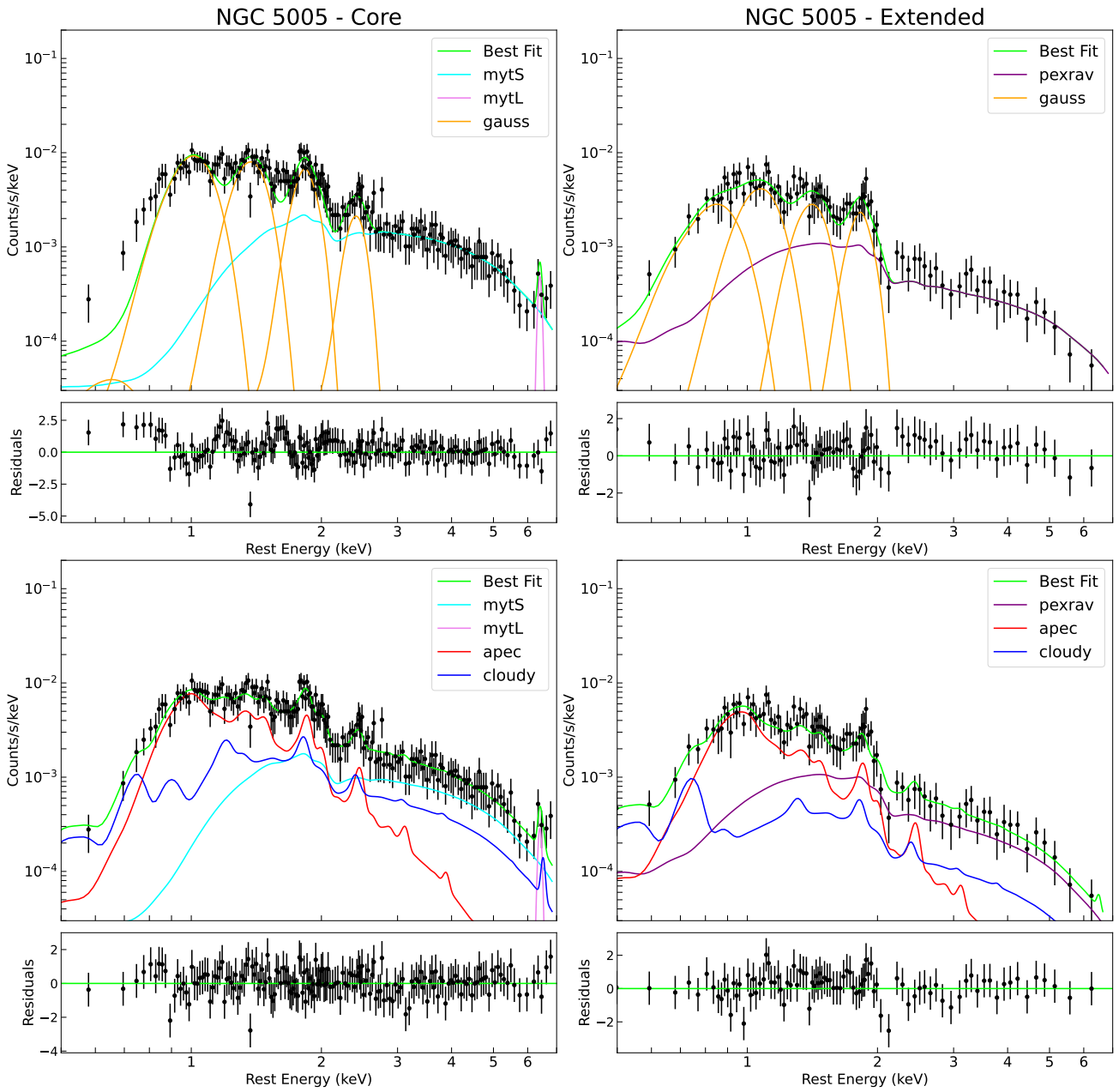


Figure 7. *Left panels:* X-ray spectrum of the core region ($r < 1.5''$), showing the best-fit phenomenological model

(top) and best-fit for a 1-photoionization + 1-thermal component model (bottom). The hard X-ray emission is modeled with a MYTorusL component for the Fe $K\alpha$ line (pink) and a MYTorusS component for the scattered continuum (cyan). *Right panel:* X-ray spectrum of the extended region ($1.5'' < r < 5''$), with the same model structure. The hard X-ray emission is modeled with an absorbed pexrav reflection component (purple).

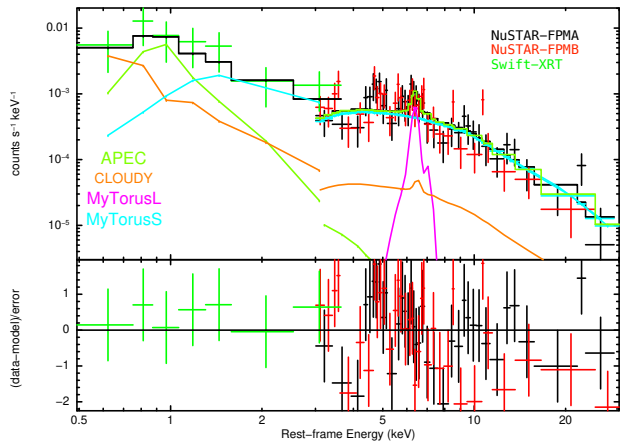


Figure 8. Joint *NuSTAR*–*Swift* spectra of NGC 5005 and best-fit model, with residuals shown below. The individual model components are indicated.

4.3. *NuSTAR*–*Swift* Spectroscopic Analysis

To complement our *Chandra* analysis, we also examined archival *NuSTAR* and *Swift* observations of NGC 5005 (Table 1, Section 2.2). The extraction regions for the *NuSTAR* and *Swift* data are shown in the right panel of Figure 6.

Figure 8 displays the unfolded (i.e., corrected for instrumental response) *NuSTAR*–*Swift* spectra, with *NuSTAR* FPMA and FPMB shown in black and red, respectively, and *Swift* XRT in green. The *Swift* data show mild excess emission at soft X-rays, while both *NuSTAR* spectra reveal the presence of a Fe K α emission line at $E_{\text{rest}} \sim 6.4$ keV. The *Swift* XRT spectrum extends up to ~ 4 keV, while the *NuSTAR* FPMA and FPMB spectra were analyzed from 3 to 30 keV, above which the background dominates.

To account for cross-calibration and extraction region differences between instruments (FPMA/B and XRT), we included a multiplicative constant²¹ component in XSPEC. The FPMA spectrum was treated as the reference, while the normalization constant for FPMB and XRT were allowed to vary. The two *NuSTAR* spectra are found to be compatible within a few percent, and the *Swift* spectrum is consistent with the *NuSTAR* FPMA data within $\sim 15\%$, as expected in a joint analysis (Madsen et al. 2015).

We first fit a simple absorbed power-law model, fixing the Galactic column density at $N_{\text{H}} = 1.18 \times 10^{20} \text{ cm}^{-2}$. This yielded a photon index of $\Gamma = 2.02 \pm 0.13$ and a fit statistic of $\text{Cstat/d.o.f.} = 0.90$. Adding a narrow Gaussian line with a fixed width of $\sigma = 50$ eV (below the resolution of *NuSTAR*) improved the fit significantly ($\Delta\text{Cstat}/\Delta\text{d.o.f.} = -15/-2$), resulting in a line centroid at $E_{\text{rest}} = 6.3 \pm 0.1$ keV and normalization of $(1.7 \pm 0.8) \times 10^{-6} \text{ photons cm}^{-2} \text{ s}^{-1}$. This model

yields an upper limit for the absorbing column of $N_{\text{H}} < 1.9 \times 10^{21} \text{ cm}^{-2}$, along with observed and intrinsic 2–10 keV source luminosities of $L_{\text{obs}}^{\text{po}} = (7.34 \pm 0.52) \times 10^{39} \text{ erg s}^{-1}$ and $L_{\text{int}}^{\text{po}} = (8.54 \pm 0.60) \times 10^{39} \text{ erg s}^{-1}$, respectively.

Next, we tested whether the best-fit model derived from the *Chandra* core region (Table 3) could describe the joint *NuSTAR*–*Swift* data. All parameters were fixed to their *Chandra* best-fit values, except for their normalizations. This model achieved a good fit ($\text{Cstat/d.o.f.} = 0.88$) and is shown in Figure 8; the best-fit parameters and 0.3–7 keV component luminosities are listed in Table 3.

The derived intrinsic luminosities for individual model components from this fit are slightly higher than in the *Chandra* core spectrum, but consistent within $\sim 2\sigma$. This difference is likely due to minor contributions from unresolved point sources within the larger apertures used for the extraction of the *NuSTAR* and *Swift* spectra (see Figure 6, right). Additionally, the mytL component normalization and luminosity are slightly enhanced compared to the *Chandra* core spectrum, which may reflect the higher effective area of the *NuSTAR* detectors in the 6–7 keV energy range.

The final best-fit model (shown in Figure 8) yields observed and intrinsic 2–10 keV luminosities of $L_{\text{obs}} = (7.62 \pm 0.45) \times 10^{39} \text{ erg s}^{-1}$ and $L_{\text{int}} = (7.91 \pm 0.44) \times 10^{39} \text{ erg s}^{-1}$, consistent with those obtained with the simpler absorbed power-law model.

5. DISCUSSION

It is well established that AGNs are powered by the accretion of material onto supermassive black holes (SMBHs) located at the centers of galaxies (Rees 1984). The diversity observed in AGN emission spectra is often attributed to differences in nuclear obscuration and the observer’s line of sight, as described by the AGN unification model (see Netzer 2015 for a review). AGNs also play a key role in galaxy evolution by injecting energy and momentum into the host galaxy through radiation, relativistic jets, and outflows, thereby influencing star formation processes (e.g., Sazonov et al. 2004).

High-resolution observations of nearby AGNs with *Chandra* have enabled studies of AGN–host galaxy interactions on spatial scales ranging from several kiloparsecs down to a few hundred parsecs. In particular, imaging and spectroscopic observations of local Seyfert galaxies (e.g., NGC 4151, Wang et al. 2011b,a,c; Mrk 573, Paggi et al. 2012; ESO 428–G014, Fabbiano et al. 2018, 2019; NGC 5728, Trindade Falcão et al. 2023, 2024a,b) have revealed the co-existence of AGN-photoionized clouds and gas shock-heated by radio jets. Our investigation of NGC 5005 builds on this line of work. Below, we explore the physical conditions in the core and extended regions using constraints from our analysis. The spatial and spectral properties of the emission help constrain the compo-

²¹ <https://heasarc.gsfc.nasa.gov/xanadu/xspec/manual/node249.html>

sition of the ISM (Section 5.1) and provide insights into the nature of the central source (Section 5.2).

5.1. Physical Properties of the Circumnuclear X-ray Gas

The 0.3–7 keV spectra of both the core and extended *Chandra* regions of NGC 5005 reveal a relatively flat continuum and multiple partially blended emission lines at soft energies (<3 keV; Figure 7). Thanks to the deep cumulative *Chandra* exposure, we are able to clearly distinguish the inner core region ($r \lesssim 1.5''$, $\lesssim 150$ pc) from the more extended region ($r = 1.5''$ – $5''$, 150–500 pc).

The core spectrum is best described by a MYTORUS reflection model (scattered + fluorescent line emission), with a fixed photon index of $\Gamma = 1.8$, which dominates the emission above 3 keV. At softer energies, the emission is well reproduced by a two-component model: a photoionized component and a collisionally ionized thermal plasma.

The primary spectral difference between the core and extended regions lies in the need for the scattered continuum and Fe $K\alpha$ fluorescence components in the core spectrum. In contrast, the extended emission is adequately modeled with a single pexrav reflection continuum at high energies.

In Figure 9, we compare the spatial distribution of optical excitation derived from spatially-resolved *HST* data (left; from Trindade Falcão et al. 2025) with the 0.3–7 keV *Chandra* image of NGC 5005 (right). The inner circle marks the core extraction region ($r < 1.5''$), and the outer circle marks the extended extraction annulus ($1.5'' < r < 5''$). In the excitation map (left), orange denotes LINER-like excitation, blue H II (star-forming)-like, green Seyfert-like, and white cocoon-like emission, corresponding to higher excitation LINER-like values in the S-BPT diagram (Trindade Falcão et al. 2025). Black pixels represent regions below the 3σ detection threshold.

Within the core region, we detect a Seyfert-like nucleus (green) coinciding with the hard X-ray peak, surrounded by cocoon-like (white) and H II-like (blue) regions. The Seyfert-like nucleus likely drives the need for a photoionized X-ray component in the core, while the cocoon and H II-like regions are consistent with thermal plasma emission. In the extended region, LINER-like excitation (orange) dominates, with localized H II-like contribution. In Trindade Falcão et al. (2025), we argued that this extended LINER-like emission may be powered by a low-luminosity AGN, consistent with the presence of a photoionized component in the extended X-ray spectrum. The thermal component may originate from shock-heated gas in the NLR, as proposed by Terao et al. (2016).

Our spectral modeling (Section 4) confirms the presence of thermal components in both the core and extended regions, with $kT \sim 0.90$ keV (Figure 7; Table 3). This temperature corresponds to a shock velocity of $v \sim 870$ km s $^{-1}$, assuming

Table 4. Thermal Gas Parameters for NGC 5005

Parameter	Core	Extended
kT (keV)	0.90 ± 0.04	0.89 ± 0.05
Volume V (10^{63} cm 3)	0.4	15
Electron density n_e ($10^{-2} \eta^{-1/2}$ cm $^{-3}$)	86.1 ± 6.7	7.3 ± 0.3
Gas mass M_{gas} ($10^5 \eta^{1/2} M_{\odot}$)	2.5 ± 0.2	7.6 ± 2.6
Thermal energy E_{th} ($10^{53} \eta^{1/2}$ erg)	7.7 ± 1.0	23 ± 1.8
Cooling time t_{cool} ($10^6 \eta^{-1/2}$ yr)	1.9 ± 0.5	22 ± 4.2

$v_{\text{shock}}^2 = 16kT_{\text{shock}}/3\mu$ (where k is the Boltzmann constant and μ is the mean molecular mass of a fully ionized gas; e.g., Travascio et al. 2021). Such shocks could arise from jet–ISM interactions or starbursts-driven winds, as suggested in Trindade Falcão et al. 2025.

We estimate the physical parameters of the thermal gas assuming a simple spherical geometry for the core region and a spherical shell for the extended region. The resulting quantities, as a function of the volume filling factor η , are summarized in Table 4. Derived electron densities range from $0.073\eta^{-1/2}$ to $0.86\eta^{-1/2}$ cm $^{-3}$, consistent with typical ISM values in AGN host galaxies (e.g., Baldi et al. 2006; Fabbiano et al. 2018; Trindade Falcão et al. 2024b).

For the core, the thermal energy content is $E_{\text{th}} = 7.7\eta^{1/2} \times 10^{53}$ erg, with a radiative cooling time of $t_{\text{cool}} = 1.9\eta^{-1/2} \times 10^6$ yr. Maintaining this temperature would require an energy injection rate of $E \sim 1.3 \times 10^{40}$ erg s $^{-1}$. Alternatively, the same energy could be supplied by $\sim 7,730\eta^{1/2}$ supernovae, assuming a 10% thermalization efficiency (Chevalier & Clegg 1985; Thornton et al. 1998), corresponding to a supernova rate of $\sim 4.0\eta^{1/2} \times 10^{-3}$ yr $^{-1}$.

To evaluate whether a recent supernova burst could contribute to the observed thermal X-ray emission in the core, we examined the optical color distribution using *HST* imaging. Specifically, we revisited the F547M/F814W color map from Trindade Falcão et al. (2025, Fig. 1), which traces blue-to-red continuum variations. Figure 10 displays the inner region of this color map, with the X-ray core extraction region overlaid. Regions strongly affected by dust extinction appear as dark red. While some reddening is expected due to dust lanes, the diffuse emission within $r = 1.5''$ (white circle) is slightly bluer (mean F547M/F814W ratio ~ 0.28). Furthermore, *HST*/STIS spectroscopy of NGC 5005 (e.g., Cazzoli et al. 2018) reveals Balmer absorption features characteristic of a post-starburst phase (e.g., Dressler & Gunn 1983), hinting at the presence of a young or intermediate-age stellar population in the nuclear region.

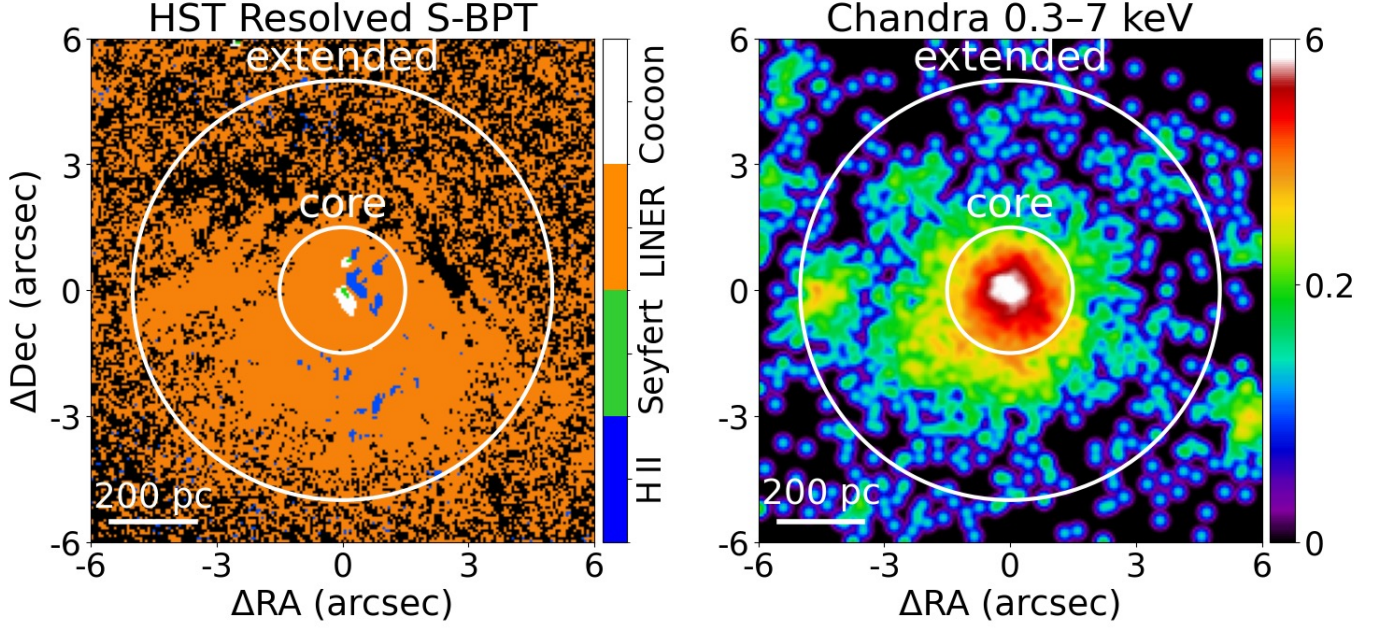


Figure 9. *Left panel:* Excitation map constructed from *HST* narrow-band imaging, showing spatially resolved emission-line diagnostics. Seyfert-like regions are shown in green, H II-like in blue, LINER-like in orange, and cocoon-like in white. *Right panel:* *Chandra* 0.3–7 keV image, binned to 1/8 of the native ACIS pixel scale. In both panels, the inner white circle marks the nuclear (core) spectral extraction region, while the outer annulus delineates the extended extraction region.

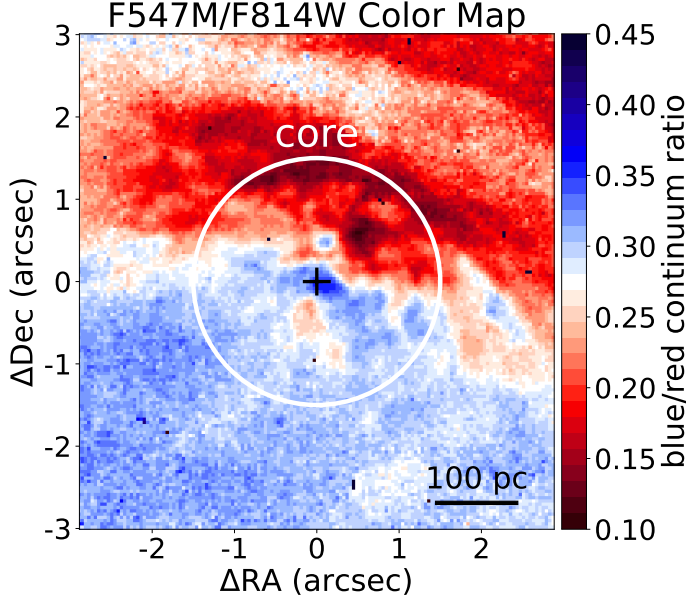


Figure 10. Color map derived from the *HST* F547M/F814W ratio, tracing the blue-to-red continuum variation across the central region of NGC 5005 (Trindade Falcão et al. 2025). Dark red regions indicate areas with significant dust extinction. The circle has a radius of $1.5''$ and marks the *Chandra* core extraction region, while the black cross marks the position of the *Chandra* 0.3–7 keV centroid.

In the extended region, we estimate a thermal energy of $E_{\text{th}} = 2.3\eta^{1/2} \times 10^{54}$ erg, which requires an energy injection rate of $E \sim 3.3 \times 10^{39}$ erg s^{-1} to maintain its observed temperature.

5.2. True Nature of the Central Source

The low observed 2–10 keV luminosities derived from both the *Chandra* core spectrum and the joint *NuSTAR–Swift* fit suggests one of three possible scenarios for the central engine in NGC 5005: (1) the AGN is heavily obscured, (2) the AGN has recently switched off, or (3) the AGN is intrinsically faint. These scenarios are illustrated schematically in Figure 11.

In the sections that follow, we evaluate each possibility in light of our spectral modeling results, aiming to better constrain the physical nature of the nuclear source in NGC 5005.

5.2.1. A Heavily Obscured AGN?

From the *Chandra* core spectrum (Section 4.2.1), we derive an observed 2–10 keV luminosity of $L_{\text{obs}} = (2.67 \pm 0.46) \times 10^{39}$ erg s^{-1} and an absorbing column density of $N_{\text{H}} = (3.7 \pm 0.3) \times 10^{21}$ cm^{-2} . This results in an intrinsic luminosity nearly identical to the observed one, $L_{\text{int}} = (2.77 \pm 0.46) \times 10^{39}$ erg s^{-1} .

The joint *NuSTAR–Swift* fit (Section 4.3) yields slightly higher luminosities, $L_{\text{obs}} = (7.62 \pm 0.45) \times 10^{39}$ erg s^{-1} and $L_{\text{int}} = (7.91 \pm 0.44) \times 10^{39}$ erg s^{-1} , with a similarly low column density of $N_{\text{H}} < 1.9 \times 10^{21}$ cm^{-2} . The modest increase in luminosity likely reflects contamination from nearby sources within the larger extraction regions (Figure 6, right).

Both fits consistently indicate low absorption, with column densities on the order of 10^{21} cm^{-2} , strongly suggesting that the nucleus of NGC 5005 is not heavily obscured. Further supporting this conclusion, the equivalent width of the neutral

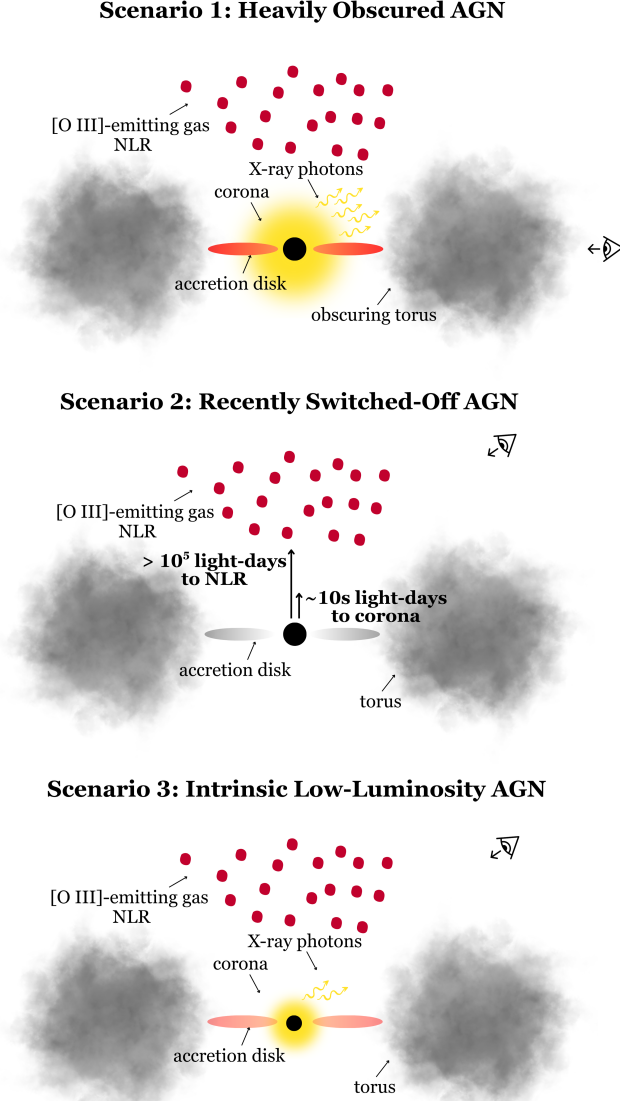


Figure 11. Summary of possible scenarios for the nature of the central engine in NGC 5005. The panels illustrate three hypotheses: (1) a heavily obscured AGN, in which strong absorption could suppress the intrinsic X-ray luminosity; (2) a recently switched-off AGN, where the central engine has faded but [O III] emission from the extended narrow-line region persists; and (3) an intrinsically low-luminosity AGN, where the central source is faint due to low accretion activity. All three scenarios are considered to explain the low observed X-ray luminosity derived from our spectral modeling.

Fe $K\alpha$ line derived from the joint *NuSTAR–Swift* fit is $EW = 287 \pm 100$ eV, well below the ~ 1 keV typically expected for Compton-thick AGN.

5.2.2. A Recently Switched-off AGN?

In AGNs, the hard X-ray continuum originating from the corona can vary on short timescales (days to months), reflecting the compact size of the emitting region (e.g., Wilkins

et al. 2014; Ricci et al. 2020). In contrast, the [O III] emission is produced in the more extended NLR and responds to changes in the central engine on much longer timescales (hundreds to thousands of years). As a result, when an AGN switches off, the coronal X-ray emission fades rapidly, while the [O III] luminosity remains elevated for some time (see Figure 11). A recently faded AGN is thus expected to exhibit a large discrepancy between its measured X-ray luminosity and that inferred from [O III] emission.

In Trindade Falcão et al. (2025), we reported an extinction-corrected [O III] luminosity of $L_{[\text{O III}]} = 1.2 \times 10^{39}$ erg s $^{-1}$. Using the $L_{[\text{O III}]}-L_X$ relation from Lamastra et al. (2009), this corresponds to an expected observed X-ray luminosity of $L_{\text{obs}} = 1.3 \times 10^{40}$ erg s $^{-1}$, consistent within uncertainties with the value derived from our joint *NuSTAR–Swift* fit.

This agreement suggests that the central engine of NGC 5005 has not recently switched off. Instead, the evidence points to the presence of an intrinsically low-luminosity AGN.

5.3. An Intrinsically Low-Luminosity AGN

Using the observed 2–10 keV X-ray luminosity derived from the joint *NuSTAR–Swift* spectral fit, and applying the bolometric correction from Duras et al. (2020), we estimate a bolometric luminosity of $L_{\text{bol}} = (1.2 \pm 0.1) \times 10^{41}$ erg s $^{-1}$. This value is consistent with the [O III]-based bolometric luminosity estimate from Trindade Falcão et al. (2025), $L_{\text{bol}} = (1.0 \pm 0.7) \times 10^{41}$ erg s $^{-1}$.

Adopting a black hole mass of $\log M_{\text{BH}} = 8.27 M_{\odot}$ from Beifiori et al. (2009), we calculate an Eddington ratio of $\lambda_{\text{Edd}} = L_{\text{bol}}/L_{\text{Edd}} \sim 5.1 \times 10^{-6}$, firmly placing NGC 5005 within the low-luminosity AGN (LLAGN) regime.

To further test this interpretation, we compare the emission-line fluxes predicted by photoionization models to the observed emission-line ratios on the spatially resolved S-BPT diagram from Trindade Falcão et al. (2025) (see Figure 12). The photoionization model adopts a configuration similar to that of Zhu et al. (2023), but utilizes an AGN SED tailored to the broadband properties of NGC 5005.

As shown in Figure 12, the model successfully reproduces most of the LINER-like emission observed in this galaxy. The only exceptions are pixels with unusually high [S II]/ $H\alpha$ ratios ($\log([S II]/H\alpha) > 0.4$), which are rare among SDSS galaxies (e.g., Kewley et al. 2006). These may reflect an underestimation of the $H\alpha$ flux due to contamination from [N II] in the *HST* narrow-band filter used in the original map (Trindade Falcão et al. 2025).

Overall, the consistency between photoionization model predictions and the observed emission-line ratios strongly supports the interpretation that NGC 5005 hosts an intrinsically faint, low-accretion-rate AGN.

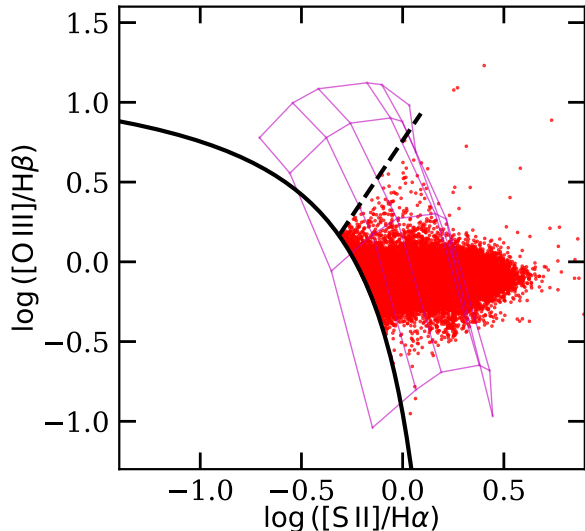


Figure 12. Comparison between the AGN photoionization model tailored to NGC 5005 (magenta grid) and the observed LINER-classified pixels (red dots) on the S-BPT diagram (Trindade Falcão et al. 2025). The model grid includes lines of constant metallicity (from left to right: $12 + \log(\text{O}/\text{H}) = 7.99, 8.28, 8.43, 8.54, 8.70, 8.80, 8.96, 9.09$) and lines of constant ionization parameter (from bottom to top: $\log U = -4.0, -3.5, -3.0, -2.5$).

5.4. A Low Accretion Rate AGN Broad-Line Region

Theoretical models predict that the broad-line region (BLR) disappears at low accretion rates or bolometric luminosities. In the model proposed by Nicastro (2000), a disk wind capable of launching the BLR can only form if the accretion rate exceeds $\dot{m} \gtrsim 10^{-3}$. Similarly, Baskin & Laor (2017) suggest that dusty photoionized gas can suppress BLR formation below $\dot{m} < 6.5 \times 10^{-4} (Z/Z_{\odot})^{-1}$, particularly in low-metallicity environments.

Using $\dot{m} = L_{\text{bol}}/(\eta c^2)$, and adopting $L_{\text{bol}} = 1.2 \times 10^{41} \text{ erg s}^{-1}$ (Section 5.3) and a standard radiative efficiency of $\eta = 0.1$, we obtain $\dot{m} \approx 2.1 \times 10^{-5} M_{\odot} \text{ yr}^{-1}$. This inferred accretion rate lies well below both thresholds, indicating that NGC 5005 is unlikely to host a BLR.

This expectation is seemingly at odds with some observational claims of a broad $\text{H}\alpha$ emission line in the optical spectrum (e.g., Balmaverde & Capetti 2014; Cazzoli et al. 2018). Constraints from *HST* spectroscopy place an upper limit on the luminosity of this broad $\text{H}\alpha$ component, $L_{\text{H}\alpha, \text{b}} < 4.2 \times 10^{38} \text{ erg s}^{-1}$ (Balmaverde & Capetti 2014). This upper limit is consistent (within uncertainties) with predictions from empirical type 1 AGN scaling relations (Stern & Laor 2012a,b), which yield an expected luminosity range of $(2.2 \pm 1.5) \times 10^{38} < L_{\text{H}\alpha, \text{b}} < (6.0 \pm 1.0) \times 10^{38} \text{ erg s}^{-1}$.

Similar challenges to the standard accretion paradigm have been reported in other systems. For example, Bianchi et al. (2019) identified a relativistically broadened $\text{H}\alpha$ line in

NGC 3147, interpreted as emission from a thin accretion disk, despite its low Eddington ratio of $\lambda_{\text{Edd}} \sim 10^{-4}$. Such detections challenge the canonical view that AGNs transition to an optically thin, geometrically thick accretion flow at low accretion rates (e.g., Blandford & Begelman 1999), and suggest that standard thin disks may persist even in the low-luminosity regime.

6. SUMMARY AND CONCLUSIONS

We present results from a deep 255 ks *Chandra* ACIS observation of NGC 5005, a LINER-dominated galaxy previously reported to host broad $\text{H}\alpha$ emission. The data reveal extended X-ray emission with a roughly symmetric morphology, tracing diffuse structure out to ~ 800 pc at soft energies (< 3 keV), decreasing to ~ 400 pc at higher energies (6–7 keV). A prominent central peak in the 0.3–7 keV image, spatially coincident with a Seyfert-like nucleus identified in *HST* imaging, is interpreted as nuclear emission.

Spectral analysis of the nuclear ($r < 150$ pc) and extended ($150 < r < 500$ pc) regions reveals strong soft X-ray lines, consistent with contributions from both photoionized and collisionally ionized gas. In the nuclear region, the best-fit model includes a low-ionization ($\log U = -0.11$), low-column density ($\log N_{\text{H}} = 21 \text{ cm}^{-2}$) photoionized component and a $kT = 0.9$ keV thermal plasma. These components are likely associated with excitation by the central AGN and shock-heated gas in the surrounding cocoon- and H II-like regions (Trindade Falcão et al. 2025). The intrinsic 2–10 keV luminosity is low, $L_{\text{int}} \sim 3 \times 10^{39} \text{ erg s}^{-1}$, with minimal obscuration ($N_{\text{H}} \sim 4 \times 10^{21} \text{ cm}^{-2}$).

The extended region also requires a photoionized component with lower ionization ($\log U = -0.76$) and lower column density ($\log N_{\text{H}} = 19.4 \text{ cm}^{-2}$) than in the core, along with a similar $kT = 0.9$ keV thermal component. These findings are consistent with excitation by a low-luminosity AGN and widespread shocks in the NLR.

Our spectral modeling provides strong evidence that the nucleus of NGC 5005 is unobscured, with column densities well below those expected for Compton-thick sources. Furthermore, the agreement between the observed and [O III]-predicted X-ray luminosities (Trindade Falcão et al. 2025) rules out a recently switched-off AGN.

The bolometric luminosity inferred from the X-ray data also agrees with that derived from [O III] emission, supporting the interpretation that NGC 5005 hosts an intrinsically low-luminosity AGN. Adopting a black hole mass of $\log(M_{\text{BH}}/M_{\odot}) = 8.27$, we estimate an extremely low Eddington ratio of $\lambda_{\text{Edd}} \sim 5 \times 10^{-6}$. At such low accretion rates, standard accretion models predict the disappearance of the broad-line region. However, this is challenged by previous reports of a broad $\text{H}\alpha$ line in NGC 5005’s optical spectrum. Alongside similar findings in other systems such as NGC 3147

(Bianchi et al. 2019), our results suggest that thin accretion structures may persist even at very low accretion rates, pos-

ing a challenge to canonical models of radiatively inefficient accretion in low-luminosity AGNs.

REFERENCES

- Asmus, D., Hönig, S. F., Gandhi, P., Smette, A., & Duschl, W. 2014, *MNRAS*, 439, 1648
- Audibert, A., Riffel, R., Sales, D. A., Pastoriza, M. G., & Ruschel-Dutra, D. 2017, *Monthly Notices of the Royal Astronomical Society*, 464, 2139.
<https://doi.org/10.1093/mnras/stw2477>
- Baldi, A., Raymond, J. C., Fabbiano, G., et al. 2006, *The Astrophysical Journal*, 636, 158.
<https://dx.doi.org/10.1086/497880>
- Baldi, R. D., Williams, D. R. A., McHardy, I. M., et al. 2018, *Monthly Notices of the Royal Astronomical Society*, 476, 3478, [_eprint: https://academic.oup.com/mnras/article-pdf/476/3/3478/24507986/sty342.pdf](https://academic.oup.com/mnras/article-pdf/476/3/3478/24507986/sty342.pdf).
<https://doi.org/10.1093/mnras/sty342>
- Balmaverde, B., & Capetti, A. 2014, *Astronomy & Astrophysics*, 563, A119, publisher: EDP Sciences. <https://www.aanda.org/articles/aa/abs/2014/03/aa21989-13/aa21989-13.html>
- Baskin, A., & Laor, A. 2017, *Monthly Notices of the Royal Astronomical Society*, 474, 1970.
<https://dx.doi.org/10.1093/mnras/stx2850>
- Beifiori, A., Sarzi, M., Corsini, E. M., et al. 2009, *The Astrophysical Journal*, 692, 856.
<https://ui.adsabs.harvard.edu/abs/2009ApJ...692..856B/abstract>
- Bianchi, S., Antonucci, R., Capetti, A., et al. 2019, *MNRAS*, 488, L1. <https://dx.doi.org/10.1093/mnras/slz080>
- Blandford, R. D., & Begelman, M. C. 1999, *MNRAS*, 303, L1.
<https://dx.doi.org/10.1046/j.1365-8711.1999.02358.x>
- Brightman, M., & Nandra, K. 2011, *MNRAS*.
<https://dx.doi.org/10.1111/j.1365-2966.2011.18612.x>
- Cazzoli, S., Marquez, I., Masegosa, J., et al. 2018, *MNRAS*, 480, 1106
- Chevalier, R. A., & Clegg, A. W. 1985, *Nature*, 317, 44, iSBN: 1476-4687. <https://doi.org/10.1038/317044a0>
- Constantin, A., Shields, J. C., Ho, L. C., et al. 2015, *The Astrophysical Journal*, 814, 149, publisher: The American Astronomical Society.
<https://dx.doi.org/10.1088/0004-637X/814/2/149>
- Dressler, A., & Gunn, J. E. 1983, *The Astrophysical Journal*, 270, 7. <http://adsabs.harvard.edu/doi/10.1086/161093>
- Duras, F., Bongiorno, A., Ricci, F., et al. 2020, *Astronomy and Astrophysics*, 636, A73
- Fabbiano, G., & Elvis, M. 2024, *Handbook of X-ray and Gamma-ray Astrophysics*, 4399
- Fabbiano, G., Paggi, A., Karovska, M., et al. 2018, *ApJ*, 855, 131
- Fabbiano, G., Siemiginowska, A., Paggi, A., et al. 2019, *ApJ*, 870, 69
- Ferland, G. J., Chatzikos, M., Guzmán, F., et al. 2017, *Revista Mexicana de Astronomía y Astrofísica*, 49, 1379
- Foster, A. R., Smith, R. K., & Brickhouse, N. S. 2012, *ApJ*, 756, 128
- Fruscione, A., McDowell, J. C., Allen, G. E., et al. 2006, in *Observatory Operations: Strategies, Processes, and Systems*, ed. D. R. Silva & R. E. Doxsey, Vol. 6270 (SPIE ASTRONOMICAL TELESCOPES + INSTRUMENTATION)
- Gallo, L. C., Lehmann, I., Pietsch, W., et al. 2006, *Monthly Notices of the Royal Astronomical Society*, 365, 688.
<https://doi.org/10.1111/j.1365-2966.2005.09755.x>
- Gehrels, N., Chincarini, G., Giommi, P., et al. 2004, *The Astrophysical Journal*, 611, 1005, publisher: IOP Publishing.
<https://iopscience.iop.org/article/10.1086/422091/meta>
- González-Martín, O., Masegosa, J., Márquez, I., Guainazzi, M., & Jiménez-Bailón, E. 2009, *Astronomy & Astrophysics*, 506, 1107, number: 3 Publisher: EDP Sciences. <https://www.aanda.org/articles/aa/abs/2009/42/aa12288-09/aa12288-09.html>
- Guainazzi, M., Fabian, A. C., Iwasawa, K., Matt, G., & Fiore, F. 2005, *Monthly Notices of the Royal Astronomical Society*, 356, 295. <https://doi.org/10.1111/j.1365-2966.2004.08448.x>
- Harrison, F. A., Craig, W. W., Christensen, F. E., et al. 2013, *The Astrophysical Journal*, 770, 103, publisher: IOP Publishing.
<https://iopscience.iop.org/article/10.1088/0004-637X/770/2/103/meta>
- Ho, L. C., Filippenko, A. V., & Sargent, W. L. W. 1997, *The Astrophysical Journal Supplement Series*, 112, 315, publisher: IOP Publishing.
<https://iopscience.iop.org/article/10.1086/313041/meta>
- Huchra, J., & Burg, R. 1992, *The Astrophysical Journal*, 393, 90.
<https://ui.adsabs.harvard.edu/abs/1992ApJ...393..90H/abstract>
- Kewley, L. J., Groves, B., Kauffmann, G., & Heckman, T. 2006, *Monthly Notices of the Royal Astronomical Society*, 372, 961, [_eprint: https://academic.oup.com/mnras/article-pdf/372/3/961/2943380/mnras0372-0961.pdf](https://academic.oup.com/mnras/article-pdf/372/3/961/2943380/mnras0372-0961.pdf).
<https://doi.org/10.1111/j.1365-2966.2006.10859.x>
- Lamastra, A., Bianchi, S., Matt, G., et al. 2009, *Astronomy and Astrophysics*, 504, 73
- Madsen, K. K., Harrison, F. A., Markwardt, C. B., et al. 2015, *ApJS*, 220, 8

- Malkan, M. A., Jensen, L. D., Rodriguez, D. R., Spinoglio, L., & Rush, B. 2017, *The Astrophysical Journal*, 846, 102, publisher: The American Astronomical Society. <https://dx.doi.org/10.3847/1538-4357/aa8302>
- Murphy, K. D., & Yaqoob, T. 2009, *Monthly Notices of the Royal Astronomical Society*, 397, 1549, eprint: <https://academic.oup.com/mnras/article-pdf/397/3/1549/3748819/mnras0397-1549.pdf>. <https://doi.org/10.1111/j.1365-2966.2009.15025.x>
- Netzer, H. 2015, *Annual Review of Astronomy and Astrophysics*, 53, 365
- Nicastro, F. 2000, *The Astrophysical Journal*, 530, L65, publisher: IOP Publishing. <https://iopscience.iop.org/article/10.1086/312491/meta>
- Paggi, A., Wang, J., Fabbiano, G., Elvis, M., & Karovska, M. 2012, *ApJ*, 756, 39
- Pogge, R. W., Maoz, D., Ho, L. C., & Eracleous, M. 2000, *The Astrophysical Journal*, 532, 323, publisher: IOP Publishing. <https://iopscience.iop.org/article/10.1086/308567/meta>
- Porter, R. L., Ferland, G. J., Kraemer, S. B., et al. 2006, *PASP*, 118, 920
- Rees, M. J. 1984, *Annual Review of Astronomy and Astrophysics*, 22, 471, publisher: Annual Reviews. <https://www.annualreviews.org/content/journals/10.1146/annurev.aa.22.090184.002351>
- Ricci, C., Kara, E., Loewenstein, M., et al. 2020, *The Astrophysical Journal Letters*, 898, L1, publisher: The American Astronomical Society. <https://dx.doi.org/10.3847/2041-8213/ab91a1>
- Risaliti, G., Maiolino, R., & Salvati, M. 1999, *The Astrophysical Journal*, 522, 157, publisher: IOP Publishing. <https://iopscience.iop.org/article/10.1086/307623/meta>
- Rush, B., Malkan, M. A., Fink, H. H., & Voges, W. 1996, *The Astrophysical Journal*, 471, 190, publisher: IOP Publishing. <https://iopscience.iop.org/article/10.1086/177962/meta>
- Sakamoto, K., Baker, A. J., & Scoville, N. Z. 2000, *The Astrophysical Journal*, 533, 149. <https://dx.doi.org/10.1086/308647>
- Sazonov, S. Y., Ostriker, J. P., & Sunyaev, R. A. 2004, *Monthly Notices of the Royal Astronomical Society*, 347, 144. <https://dx.doi.org/10.1111/j.1365-2966.2004.07184.x>
- Shuder, J. M., & Osterbrock, D. E. 1981, *The Astrophysical Journal*, 250, 55. <https://ui.adsabs.harvard.edu/abs/1981ApJ...250...55S/abstract>
- Spinelli, P. F., Storchi-Bergmann, T., Brandt, C. H., & Calzetti, D. 2006, *The Astrophysical Journal Supplement Series*, 166, 498, publisher: IOP ADS Bibcode: 2006ApJS..166..498S. <https://ui.adsabs.harvard.edu/abs/2006ApJS..166..498S>
- Stern, J., & Laor, A. 2012a, *Monthly Notices of the Royal Astronomical Society*. <https://dx.doi.org/10.1111/j.1365-2966.2012.20901.x>
- . 2012b, *Monthly Notices of the Royal Astronomical Society*. <https://dx.doi.org/10.1111/j.1365-2966.2012.21772.x>
- Terao, K., Nagao, T., Hashimoto, T., et al. 2016, *ApJ*, 833, 190
- Thornton, K., Gaudlitz, M., Janka, H.-T., & Steinmetz, M. 1998, *The Astrophysical Journal*, 500, 95. <https://dx.doi.org/10.1086/305704>
- Travascio, A., Fabbiano, G., Paggi, A., et al. 2021, *ApJ*, 921, 129
- Trindade Falcão, A., Fabbiano, G., Elvis, M., Paggi, A., & Maksym, W. P. 2023, *ApJ*, 950, 143
- . 2024a, *ApJ*, 963, 6
- . 2024b, *The Astrophysical Journal*, 977, 275, publisher: IOP Publishing. <https://iopscience.iop.org/article/10.3847/1538-4357/ad8de3/meta>
- Trindade Falcão, A., Fabbiano, G., Elvis, M., et al. 2025, *The Astrophysical Journal*, 986, 175, publisher: IOP Publishing. <https://iopscience.iop.org/article/10.3847/1538-4357/addc64/meta>
- Véron-Cetty, M.-P., & Véron, P. 2006, *Astronomy & Astrophysics*, 455, 773, number: 2 Publisher: EDP Sciences. <https://www.aanda.org/articles/aa/abs/2006/32/aa5177-06/aa5177-06.html>
- Wang, J., Fabbiano, G., Elvis, M., et al. 2011a, *The Astrophysics Journal*, 736, 62
- Wang, J., Fabbiano, G., Risaliti, G., et al. 2011b, *The Astrophysics Journal*, 729, 75
- Wang, J., Fabbiano, G., Elvis, M., et al. 2011c, *The Astrophysics Journal*, 742, 23
- Wilkins, D. R., Kara, E., Fabian, A. C., & Gallo, L. C. 2014, *Monthly Notices of the Royal Astronomical Society*, 443, 2746. <https://doi.org/10.1093/mnras/stu1273>
- Younes, G., Porquet, D., Sabra, B., & Reeves, J. N. 2011, *Astronomy & Astrophysics*, 530, A149, publisher: EDP Sciences. <https://www.aanda.org/articles/aa/abs/2011/06/aa16806-11/aa16806-11.html>
- Younes, G., Porquet, D., Sabra, B., Reeves, J. N., & Grosso, N. 2012, *Astronomy & Astrophysics*, 539, A104, publisher: EDP Sciences. <https://www.aanda.org/articles/aa/abs/2012/03/aa18299-11/aa18299-11.html>
- Zhu, P., Kewley, L. J., & Sutherland, R. S. 2023, *The Astrophysical Journal*, 954, 175, publisher: IOP Publishing. <https://iopscience.iop.org/article/10.3847/1538-4357/acd757/meta>